13th ANKARA INTERNATIONAL AEROSPACE CONFERENCE **AIAC-2025-041**
17-19 September 2025 – METU, Ankara, TURKIYE

COMPUTATIONAL INVESTIGATION OF PERPENDICULAR BLADE-VORTEX INTERACTION

Mahmut Arican[1]
Middle East Technical University (METU)
Ankara, Türkiye

Harika S. Kahveci[2]
Middle East Technical University (METU)
Ankara, Türkiye

ABSTRACT

Blade-vortex interaction is a complex flow phenomenon where a rotor blade encounters a vortex flow shed by a preceding blade, drastically changing the aerodynamics of the blade and the structure of the vortex. Investigation of intricate flow features in vortex interactions with aerodynamic surfaces is crucial since this phenomenon influences the aerodynamic performance. Although such flows exhibit unsteady features, steady-state analyses are performed in this investigation with the aim of reducing the computational expense since they can still offer sufficient resolution if a highly refined grid is used. This study investigates the flow field under the influence of perpendicular blade-vortex interaction (BVI) by using Reynolds-averaged Navier-Stokes (RANS) equations, where the vortices are formed by a vortex generator located upstream of an airfoil. The angle of attack of the vortex generator is incrementally varied over a range of ±10° while the downstream airfoil is kept fixed at the given position and orientation. Results demonstrate how the vorticity field at different locations throughout the domain and the skin friction and pressure coefficients around the airfoil surface are affected by different angle of attack values of the upstream vortex generator, bringing more insight into the influence of vortex flow behavior on the flow field around an aerodynamic surface. The angle of attack of the vortex generator is found to be strongly dictating the vortex strength, trajectory, and rotational direction of vortices, which leads to distinct attachment and separation patterns on the airfoil surfaces. A pronounced effect of the impacting vortex on the airfoil surface is observed on its skin friction and pressure distributions resulting in observable variations along the airfoil span, which is further examined via a follow-up aerodynamic performance analysis.

INTRODUCTION

Vortex–surface interactions have been studied both experimentally and numerically in a variety of areas such as rotary-wing aerodynamics, fixed-wing and combat aircraft, missile and projectile aerodynamics, turbomachinery, and wind turbines. Wittmer et al. [Wittmer, Devenport, Rife and Glegg, 1995] studied the perpendicular blade vortex interaction between a streamwise vortex and a spanwise-oriented blade, which creates complex unsteady aerodynamic effects. It was observed that this interaction was causing an immediate loss in vortex core circulation, an increase in the core radius, and a decrease in the peak tangential velocity. Such interactions of a vortex core with several subsequent blades contribute to the broadband noise in helicopters during level flight or mild climbs. Chen and Chiou [Chen and Chiou, 1998] experimentally investigated the unsteady interaction between a parallel vortex

[1] M.Sc. Student in Department of Aerospace Engineering, Email: mahmut.arican@metu.edu.tr
[2] Assoc. Prof. in Department of Aerospace Engineering, Email: kahveci@metu.edu.tr

and flat plates with varying leading-edge shapes, showing the oscillating vortex generator created an alteration in the pressure distribution of the blade during the vortex interaction. Omar et al. [Omar, Chongam and Oh-Hyun, 2002] used numerical simulation to study how body-generated vortices interact with fins. The authors concluded that the fin location affects the point where vortices detach from the body, but not their upstream vortex structure and behavior. DeSpirito [DeSpirito, 2016] validated CFD predictions against wind tunnel data for vortex interactions with a downstream fin. The study found that a mesh resolution of 15–20 cells per vortex core was sufficient to capture the wake region of the upstream fin. The results showed good agreement in vortex characteristics, fin forces and reasonable agreement in vortex trajectories, although vortex intensity diffused faster in simulations. Droandi et al. [Droandi, Gibertini and Zanotti, 2016] studied the perpendicular blade-vortex interaction over an oscillating airfoil through experiment and CFD simulation. The degradation in blade performance due to vortex impingement during dynamic stall was verified by using stereoscopic PIV and CFD simulations in the study. Vortex-boundary layer interactions on a plate surface are investigated in a wind tunnel environment by Sun et al. [Sun, Gu and Zhao, 2019]. Vortex-induced separation and reattachment were observed, and the secondary vortices were identified during interaction. Colli et al. [Colli, Abbà and Gibertini, 2022] applied Large Eddy Simulation (LES) and wind tunnel tests on tandem setup wings to study parallel blade–vortex interactions. The study finds vortex impingement resulted in significant alteration of lift, drag, and pitching moment. Werner et al. [Werner, Rein, Richter and Weiss, 2023] studied vortex/vortex and vortex/shock interactions over a triple-swept delta wing under transonic speeds, both experimentally and numerically. The authors examined vortex merging and shock-induced breakdown in the study and concluded a scale-resolving Improved Delayed Detached Eddy Simulation (IDDES) results yield better agreement with experiments than unsteady RANS (URANS), particularly in capturing vortex behavior.

The accurate simulation of vortex–surface interactions, particularly those involving concentrated vortex flows, remains a critical challenge in Computational Fluid Dynamics (CFD). Concentrated vortices, characterized by coherent vorticity and strong rotational cores, play a significant role in enhancing or degrading aerodynamic performance [Luckring and Rizzi, 2024]. Capturing the physics of these flows requires high-fidelity CFD methods, where the resolution of vortex cores, shear layers, and secondary flow separations make the use of fine computational grids necessary. With an unsteady analysis of a large number of cases, resolving these features in three-dimensional domain can easily turn into a substantial computational burden.

To address this limitation, steady-state flow analyses will be utilized to capture vortex-surface interactions ensuring sufficient accuracy for the purpose of this study. For the simulations, a case of perpendicular blade-vortex interaction (BVI) formed by a vortex generator and an airfoil, which is representative of vortex interaction phenomenon encountered in rotorcraft aerodynamics, is selected. The resulting far and near-field flow features for the airfoil surface including the concentrated vortex structures will be examined in detail.

PROBLEM DESCRIPTION

To simulate the effect of the BVI phenomenon, a vortex generator and an airfoil positioned downstream of the generator are modeled. The numerical analyses are repeated over a series of cases where the angle of attack of the vortex generator is varied incrementally between +10° and -10°. The downstream airfoil's angle of attack is set to 0°.

Droandi et al. [Droandi, Gibertini and Zanotti, 2016] studied the unsteady behavior of the perpendicular BVI phenomenon. For validation of numerical model and CFD methodology, they used a vortex generator without the airfoil geometry at rear in the steady analyses. The same model with that of Droandi et al. [Droandi, Gibertini and Zanotti, 2016] is used in the current paper to make use of the experimental data they presented in their study. The model is a representation of an experimental test rig geometry. It consists of a vortex generator and an airfoil geometry in a wind tunnel environment. Both have a constant cross-section of NACA 23012 and a chord length of c = 0.3 m. The computational domain has a cross section of 0.984

m x 1.484 m. Its total length equals 32.5 c with the leading edge of the airfoil located at 11.75 c away from the domain inlet. Further details on the numerical model are given in Figure 1. The setup is exposed to a free stream velocity of U_∞ = 30 m/s. This corresponds to a Reynolds number (Re) of 600,000 based on the airfoil chord and a Mach number of 0.09.

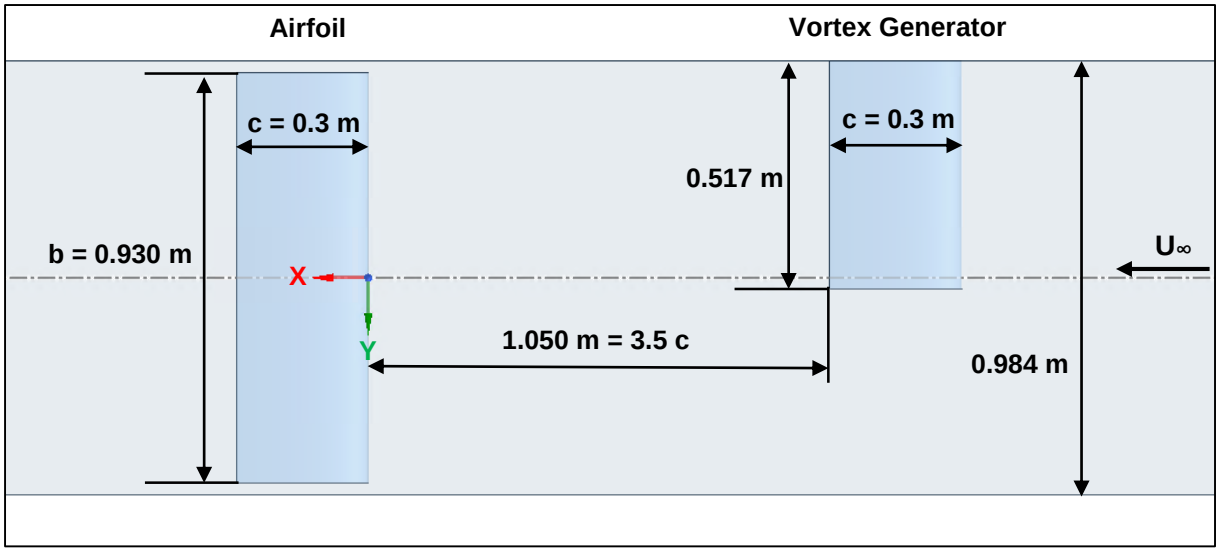

Figure 1: Model setup (top view)

METHODOLOGY

Details on the flow solver, computational domain, simulation setup and the grid used for the CFD analyses are described next in the subsequent sections.

Flow Solver

For the simulations, the commercial CFD solver ANSYS Fluent Release 2024 R2 is used to solve steady incompressible RANS equations. Since a low subsonic flow is simulated, pressure–velocity coupling numerical scheme with the Rhie–Chow momentum-based flux correction is employed to simultaneously satisfy the momentum and continuity equations with stable flux evaluation. Spatial discretization is applied using first-order, second-order, and the third-order QUICK (Quadratic Upwind Interpolation for Convective Kinematics) schemes, respectively, to achieve better convergence, higher accuracy, and reduced numerical diffusion. Time discretization is handled with second-order implicit formulation. For gradient calculation, the Green–Gauss cell-based method is selected, knowing the applied grid does not contain highly skewed cells. Further details on the employed methodologies are available in the ANSYS Fluent Theory Guide [ANSYS, Inc., 2024].

The turbulence model used for the analyses is the one-equation Spalart Almaras (SA) model [Spalart and Almaras, 1994] with the strain-vorticity based production term option enabled. The rotation – curvature correction modification derived by Spalart and Shur [1997] and Shur et al. [2000] is used to enhance the predictions of vortical flows. The correction coefficient (C_{curv}) used in that method is set to 4 in the current analysis.

Computational Domain

In the study, calculations are performed according to the flow conditions used by Droandi et al. [Droandi, Gibertini and Zanotti, 2016] to reproduce the same wind tunnel environment. The boundary names and conditions are presented in Figure 2 and Table 1, respectively.

Figure 2: Domain boundaries (top view)

Table 1: Boundary conditions

Boundary Name	Boundary Condition
Inlet	Velocity Inlet
Outlet	Pressure Outlet
Wind Tunnel Walls	Symmetry (Slip Wall)
Vortex Generator (VG) and Airfoil	Viscous Wall (No Slip)

The symmetry (slip wall) boundary condition is applied on the wind tunnel walls with the aim of reducing the computational cost, hence no boundary layers were used there. According to Droandi et al. [Droandi, Gibertini and Zanotti, 2016], no significant effects are expected by doing so.

Grid

Resolving vortex flow structure while preventing the numerical diffusion is challenging and needs a sufficiently refined computational discretization in CFD simulations. A fine and hexahedral computational grid is highly recommended in order to obtain high-fidelity RANS solutions [DeSpirito, 2016]. DeSpirito [2016] states that the numerical diffusion is diminished when the flow is aligned with the grid. Hence, a cartesian grid structure is utilized in the simulations while maintaining a structured discretization needed to resolve the vortex flow physics. The selected grid via the grid sensitivity studies is seen in a close view in Figure 3.

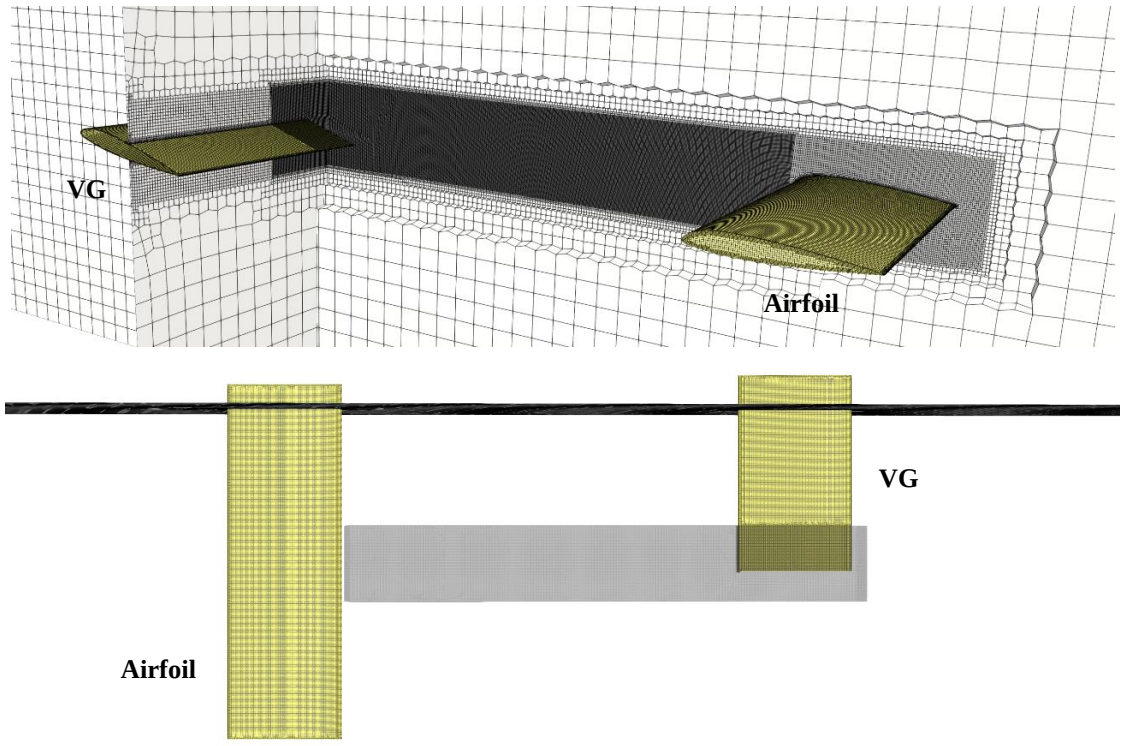

Figure 3: Details of the grid used in the study

Similar to the study of Droandi et al. [Droandi, Gibertini and Zanotti, 2016], the vortex generator is first modeled without the airfoil geometry for validation purposes. To capture the viscous wall effects, 20 layers of prism cells are created keeping the minimum spacing in the direction normal to the surfaces of both the vortex generator and the airfoil as $1x10^{-5}$ m, as suggested by Droandi et al. [Droandi, Gibertini and Zanotti, 2016]. This resulted in a dimensionless wall distance, y^+, of less than 1. To resolve the vortex core properly, the grid is refined at the downstream and tip region of the vortex generator as shown in Figure 3. The region has hex-dominated cells to ensure a uniform discretization along the vortex path. Except its tip region, the surface grid of the vortex generator has the same refinement level as that of the airfoil.

The grid generation process takes place in two steps, which is demanding but necessary for reliable results. First, for the surface and near field of the vortex generator, the refinement levels around the vortex region are determined and fixed. Then, by controlling the maximum cell size, a grid sensitivity study is carried out, and a suitable grid for the vortex generator and vortex region is selected. Later, the airfoil is added to the existing grid with the same surface refinement levels as the vortex generator, and a second grid sensitivity study is performed to ensure accuracy in the near field of the airfoil where the vortex flow interactions occur. This gives the final grid that includes the vortex generator, airfoil, and the vortex region together.

Grid Sensitivity Studies

In this section, the grid sensitivity studies are carried out for both the vortex generator and the airfoil to ensure spatial independence of the results.

Grid Sensitivity Study for Vortex Generator and Vortex Region: A grid sensitivity study is conducted to examine the sensitivity of the flow solution to field discretization, and the results are compared with the mean flow measurements [Droandi, Gibertini and Zanotti, 2016]. The selected computational grid is used to obtain grid-independent vortex flow-field results in all simulations performed.

Three computational grids are simulated for the case where the upstream vortex generator is fixed at α = 10° and without the downstream airfoil geometry. The sizes of grids #1, #2, and #3 are designated by N_1, N_2 and N_3, respectively, in Table 2. For estimation of discretization error, the procedure described by Celik et al. [Celik, Ghia, Roache, Freitas, Coleman and Raad, 2008] is applied and is described below:

Step 1: Local cell sizes are selected to be h_1 = 1.25, h_2 = 1.65625 and h_3 = 2.1875 for grids #1, #2, and #3, respectively. In the current study, this selection is done in the grid region where the vortex core is captured.

Step 2: The grid refinement factor ($r=h_{coarse}/h_{fine}$) is set to be greater than 1.3 maintaining distinct mesh sizes among the grids.

Step 3: Defining $r_{32}=h_3/h_2$ and $r_{21}=h_2/h_1$ where $h_1<h_2<h_3$, and $\varepsilon_{32} = \phi_3 - \phi_2$, $\varepsilon_{21} = \phi_2 - \phi_1$, the order of accuracy p of the method using the expression is calculated iteratively via Equations (1), (2), and (3).

$$p = \frac{1}{\ln(r_{21})} |\ln |\varepsilon_{32}/\varepsilon_{21}| + q(p)| \quad (1)$$

$$q(p) = \ln\left(\frac{r_{21}^p - s}{r_{32}^p - s}\right) \quad (2)$$

$$s = 1 \cdot \mathrm{sgn}(\varepsilon_{32}/\varepsilon_{21}) \quad (3)$$

Step 4: Next, the extrapolated values are calculated via Equation (4):

$$\phi_{\mathrm{ext}}^{21} = \left(r_{21}^p \phi_1 - \phi_2\right)/\left(r_{21}^p - 1\right) \quad (4)$$

Step 5: In the final step, the approximate relative error, extrapolated relative error, and the fine grid convergence index are estimated via Equations (5), (6), and (7), respectively:

$$e_a^{21} = \left| \frac{\phi_1 - \phi_2}{\phi_1} \right| \tag{5}$$

$$e_{\text{ext}}^{21} = \left| \frac{\phi_{\text{ext}}^{12} - \phi_1}{\phi_{\text{ext}}^{12}} \right| \tag{6}$$

$$\text{GCI}_{\text{fine}}^{21} = \frac{1.25 e_a^{21}}{r_{21}^p - 1} \tag{7}$$

Table 2: Discretization error calculations

	ϕ = Max vorticity magnitude [1/s] at x/c=0	ϕ = Pressure at max vorticity magnitude [Pa] at x/c = 0
$N_1 - N_2 - N_3$	32,957,908 – 15,096,083 – 6,968,905	32,957,908 – 15,096,083 – 6,968,905
r_{21}	1.325	1.325
r_{32}	1.321	1.321
ϕ_1	3,198.3	92,277
ϕ_2	3,087.3	92,276
ϕ_3	2,806	92,303
p	3.367	11.84
${\phi_{ext}}^{21}$	3,268.6	92,277.04
${e_a}^{21}$	3.47%	0.0011%
${e_{ext}}^{21}$	2.15%	0.00001%
${GCI_{fine}}^{21}$	2.75%	0.0001%

Calculations are carried out for maximum vorticity magnitude value at x/c=0 plane and pressure at the same location. For grid #1 (fine grid), the grid convergence index (GCI) values suggest numerical uncertainties of 2.75% for the maximum vorticity magnitude and an almost 0 value (0.0001%) for the pressure.

Figure 4 shows the comparison of the non-dimensional velocity profiles at the airfoil leading edge (x/c = 0) predicted by CFD in the current study with the experimental results. Y_v and Z_v are the coordinates of the vortex core center where the magnitude of the vorticity reaches its maximum value on the plane. All three grids give a similar and satisfactory agreement with the experimental velocity profile for the velocity component w, while grids #1 (fine) and #2 (medium) better capture the peaks of the velocity components v and w. Since the results with grids #1 and #2 differ only slightly, grid #2 which has 15,096,083 cells is selected for subsequent analysis to reduce computational cost.

Predictions of concentrated vortex structure can be seen clearly in the following vorticity contours in Figure 5 and Figure 6. Here, x-component of the vorticity is designated by Ω_x and the y-component by Ω_y. For comparison, these results are demonstrated in the same scale and using the same iso-surface of Q-criterion, Q, as was done by Droandi et al. [Droandi, Gibertini and Zanotti, 2016], which is used to effectively visualize the vortex structure of the flow field. The vorticity distributions and magnitudes are found to be reasonably similar to those obtained by Droandi et al. [Droandi, Gibertini and Zanotti, 2016]. As a result, it was concluded that this CFD methodology accompanied with grid # 2 can be used to ensure the accuracy of the vortex flow travelling toward downstream. In these figures, the x/c = 0 position shows the leading edge of the downstream airfoil (not shown in the figure). The trailing edge of the vortex generator corresponds to a position of x/c = -3.5 (see Figure 1).

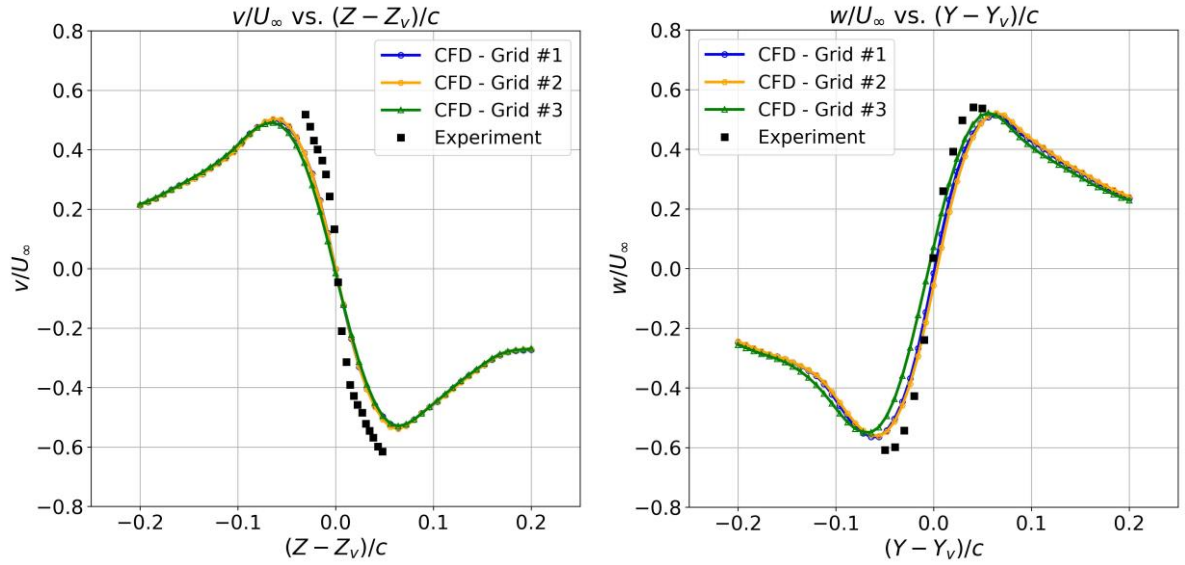

Figure 4: Velocity profiles at vortex core on y-z planes at x/c = 0 (experiment by Droandi et al. [Droandi, Gibertini and Zanotti, 2016])

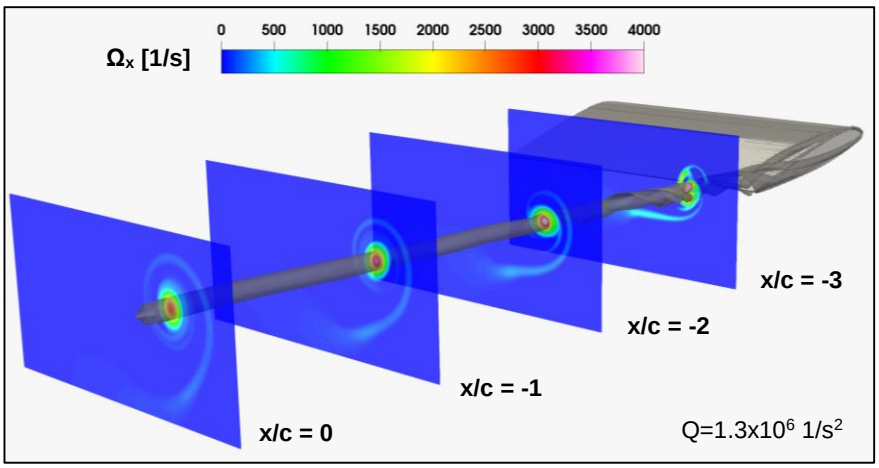

Figure 5: X-component of vorticity on y-z planes with VG at α = 10°

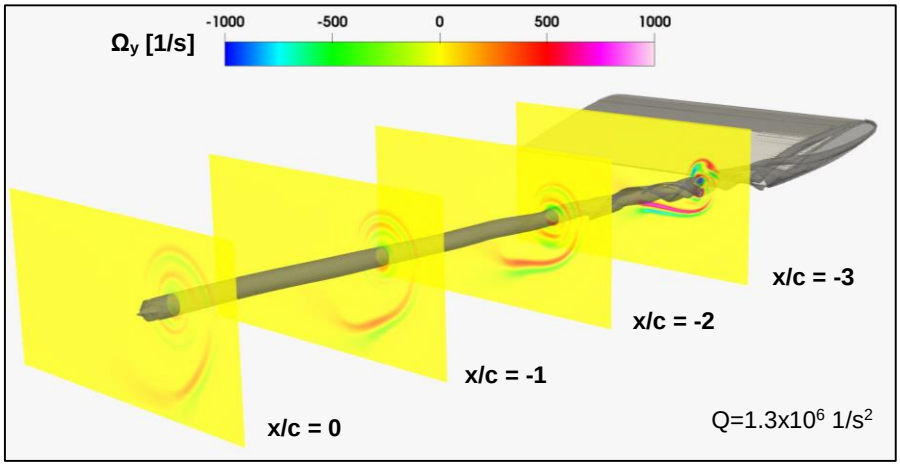

Figure 6: Y-component of vorticity on y-z planes with VG at α = 10°

A more detailed look at the vortex structures in the flow stemming from the vortex generator that was shown in Figure 5 is given in Figure 7. Since the vortex generator is a finite wing with a NACA23012 cross-section and a flat tip, it can be seen that several sharp-edge separations start from the leading edge and continue toward the trailing edge. Along the surface of the vortex generator, multiple vortex cores form due to this sharp-edge separation, following a helical trajectory and gradually merging into a single core further downstream of the vortex generator. In Figure 7, at around x/c = -2 (a distance of 2.5 chord length from the leading edge), it is observed that the vortices are fully merged into a single vortex.

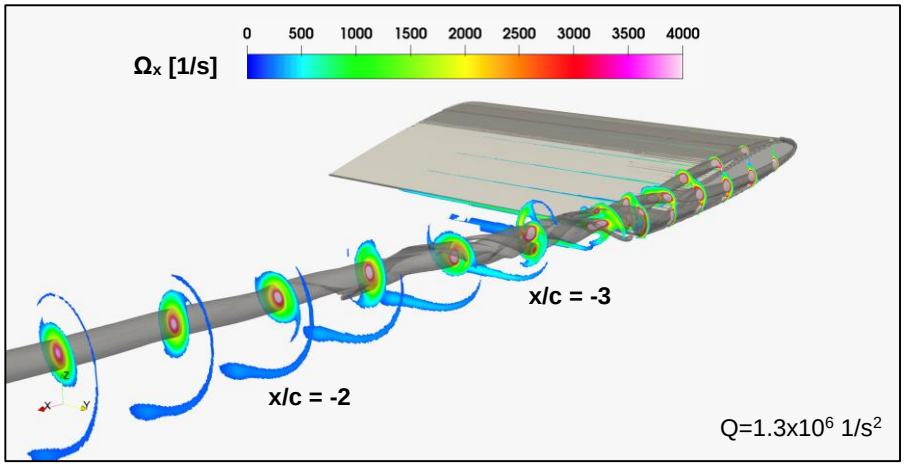

Figure 7: Detailed flow field demonstrating the x-component of vorticity on y-z planes with VG at α = 10°

Grid Sensitivity Study for Airfoil: To investigate the vortex–airfoil interaction, an additional grid sensitivity study is conducted with focus on the near-field region of the airfoil. In this study, the grid obtained in the previous step including the vortex generator and the whole domain with the volume grid is extended to now include the grid for the downstream airfoil. The grid around the airfoil is refined progressively, level by level, to ensure adequate spatial discretization for resolving the interaction phenomenon.

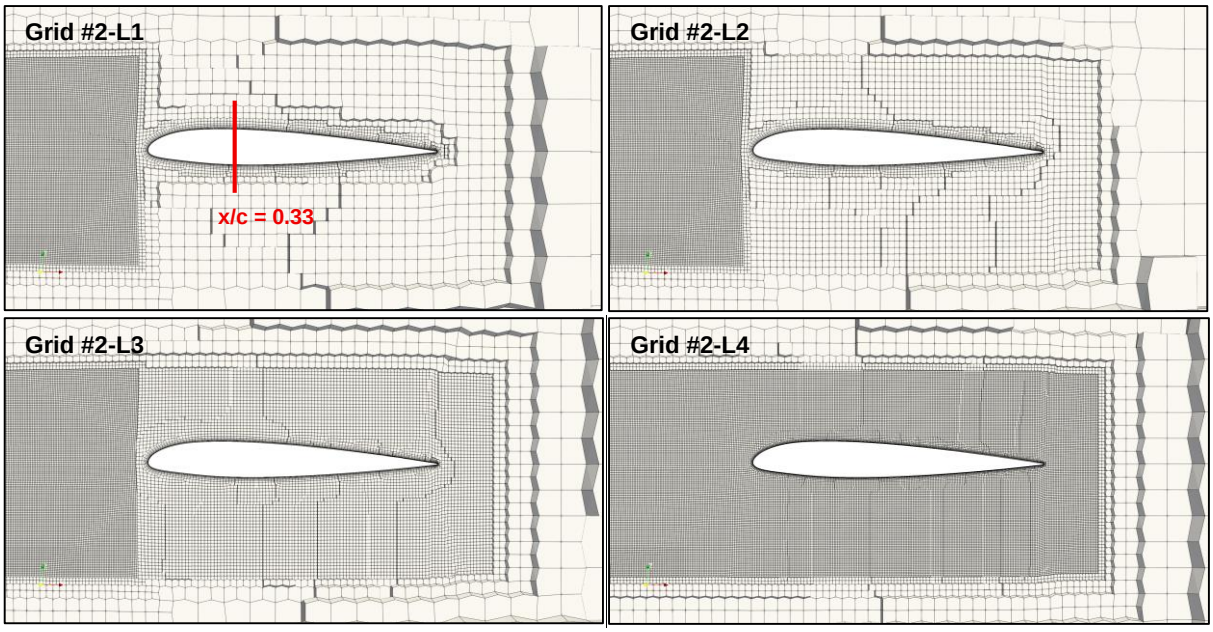

Figure 8: Grid refinement levels studied for the airfoil

Figure 8 presents the grid configurations corresponding to the case with the upstream vortex generator fixed at 10° and the downstream airfoil set at an angle of α = 0°, showing the differences in the refinement levels. At each refinement level, the cell size is reduced by a factor of 0.5 relative to the previous grid. The red line indicates the cross-section corresponding to the vorticity contours that will be shown in Figure 9 next.

Table 3: Grid total cell counts

Refinement Level	# Cells
Grid #2–L1	17,064,525
Grid #2–L2	17,242,456
Grid #2–L3	18,774,969
Grid #2–L4	35,088,915

Table 3 presents the refinement levels of the airfoil region, and the corresponding total cell counts of the grid containing both the VG and the airfoil. All grids share the same cell size distribution of grid #2, except in the near-field region of the airfoil, where the refinement is varied. In this study, only the refinement level of the airfoil region is modified. Increasing the refinement beyond level 3 leads to a substantial rise in the total cell count, as the cell size at level 4 is approximately 1.65 mm, which is significantly smaller compared to the maximum cell size of 53 mm.

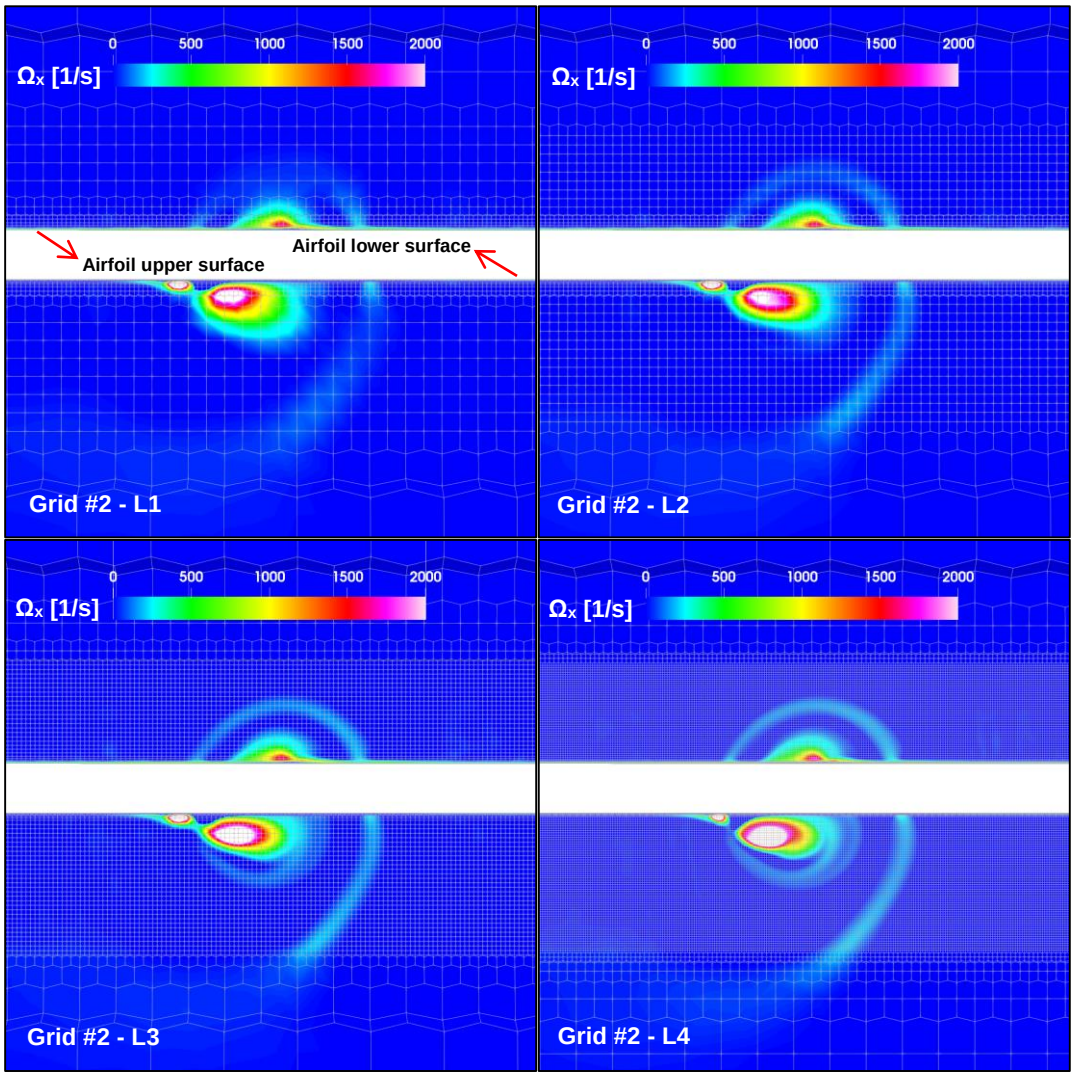

Figure 9: X-component of vorticity at x/c = 0.33 – Looking from the downstream of the airfoil

The vorticity-X contours around the airfoil are shown in Figure 9. The view is aft looking forward. The contours indicate that, beyond refinement level 3, the vortex flow field solution becomes almost independent of the grid. On the lower surface, the vortex core resolution improves with increasing refinement level.

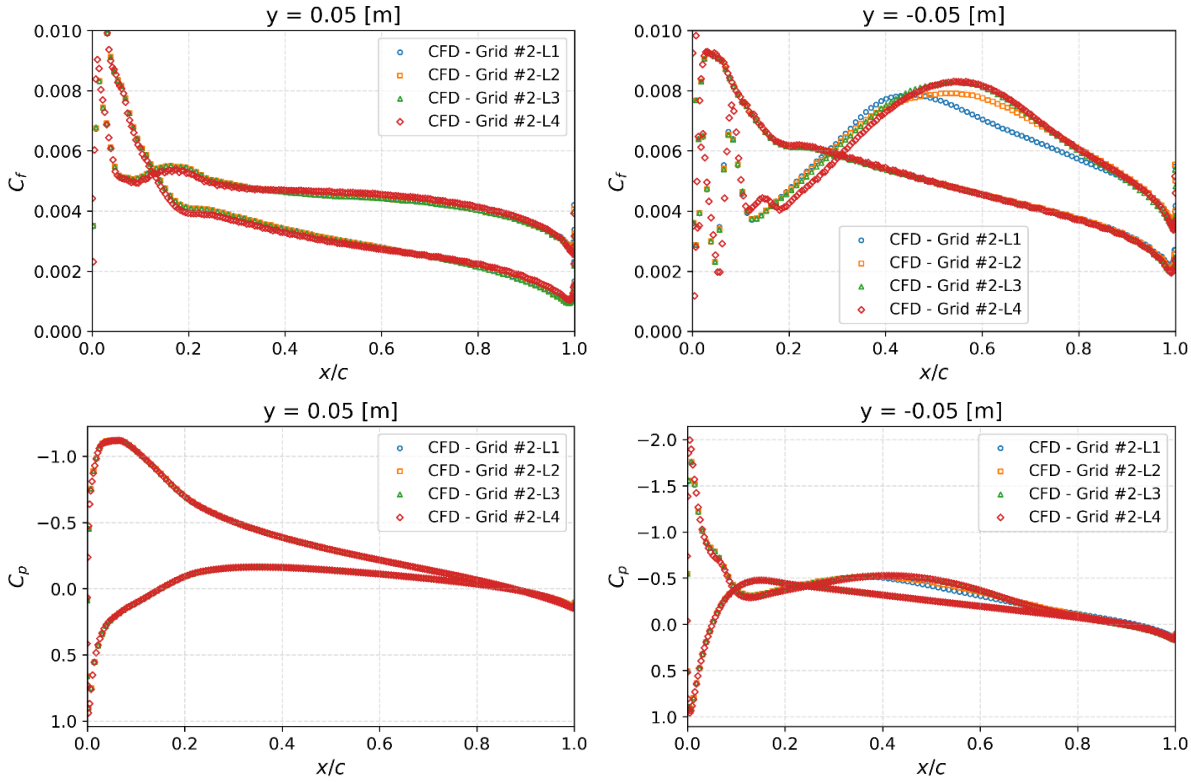

Figure 10: Comparisons along the chord of the airfoil at y = ±0.05 m,
top row: skin friction coefficient, bottom row: pressure coefficient

Figure 10 presents the chordwise distributions of the skin friction and pressure coefficients at y = ±0.05 on the airfoil surface, where the vortex flow impinges. Both sections are influenced by the impinging vortex, though with different effects. These figures also confirm that the refinement level 3 is sufficient to adequately resolve the vortex flow field around the airfoil. These surface variations are analyzed in detail in the following sections. The primary objective is to reaffirm that the chaotic nature of the flow remains independent of the grid. The selected refinement level provides sufficient resolution to capture the essential flow features.

RESULTS AND DISCUSSION

The sensitivity analyses confirm that the vortex dynamics are accurately captured in the simulations, demonstrating that spatial resolution is adequately ensured. With this numerical reliability established, the focus now shifts to the flow field visualizations of the impinging vortex. These visualizations provide detailed insight into the vortex–airfoil interaction, and the corresponding observations are discussed in terms of their influence on the aerodynamic performance of the airfoil.

The following simulations presented in this section are performed by fixing the airfoil at an angle of attack of 0° while varying the angle of attack of the vortex generator at +10°, +6°, 0°, –6°, and –10°. In addition, to emphasize the role of the vortex generator, a reference simulation is conducted without the vortex generator itself. Each figure consists of sub-figures which are the vortex generator (VG)-airfoil couple in the flow field (top left), the cross-sectional view of the vortex field at x/c = 0.33 which corresponds to the red line that was shown in Figure 8 (top

right), and a blown-up version of the VG-airfoil figure to give a closer look at the vortex structures around and in the vicinity of the airfoil surface (bottom). The white stripe passing through the contours given in the cross-sectional view is the airfoil surface in sight. The same iso-surface of Q-criterion that was used by Droandi et al. [Droandi, Gibertini and Zanotti, 2016] on the airfoil surface is used here as well. Compared to Figures 5, 6, and 7, the Q value is reduced to increase the vortex resolution on the airfoil surface.

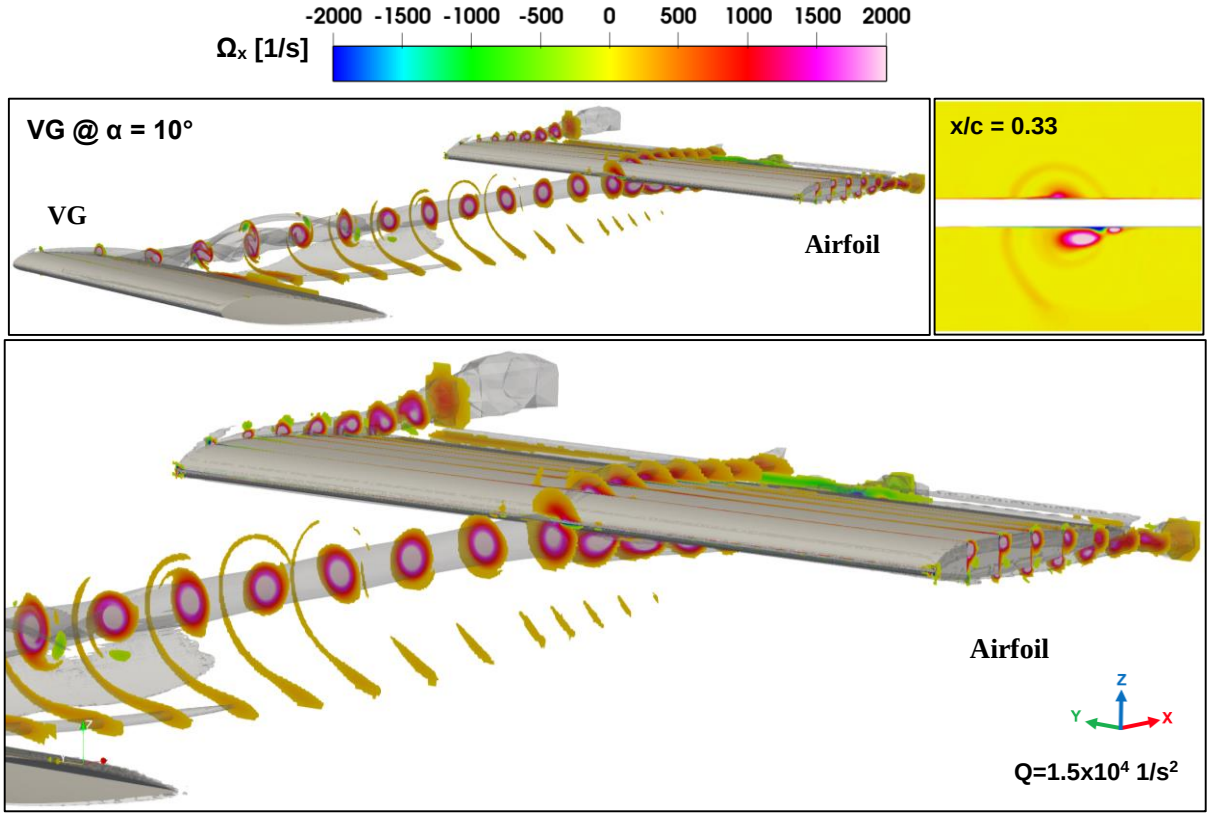

Figure 11: X-component of vorticity on y-z planes with VG at α = 10°

The x-component vorticity contours in Figure 11 clearly illustrate the rotational characteristics of the vortex structures. The rotational direction of the x-component vorticity is defined per the coordinate axes shown in Figure 1. Hence, colors corresponding to positive vorticity values represent a counterclockwise (CCW) rotation when looking from the trailing edge of the airfoil toward upstream, whereas colors corresponding to negative values indicate a clockwise (CW) rotation looking from that same direction. The rotational direction is governed by the geometry of the vortex generator, which employs a cambered NACA23012 airfoil. Even at zero angle of attack, this camber generates a pressure difference that produces lift. At the flat-ended wing tip, this pressure difference induces multiple sharp-edge separations, giving rise to concentrated vortical flows rotating in the CCW direction. As it will be shown, as the angle of attack of the vortex generator increases, the strength of these separations grows, resulting in higher vortex core vorticity. Conversely, negative angles of attack promote suction on the lower surface of the vortex generator and diminish the effective camber. This weakens the primary separation mechanism and reverses the swirling direction of the tip vortex as it develops downstream.

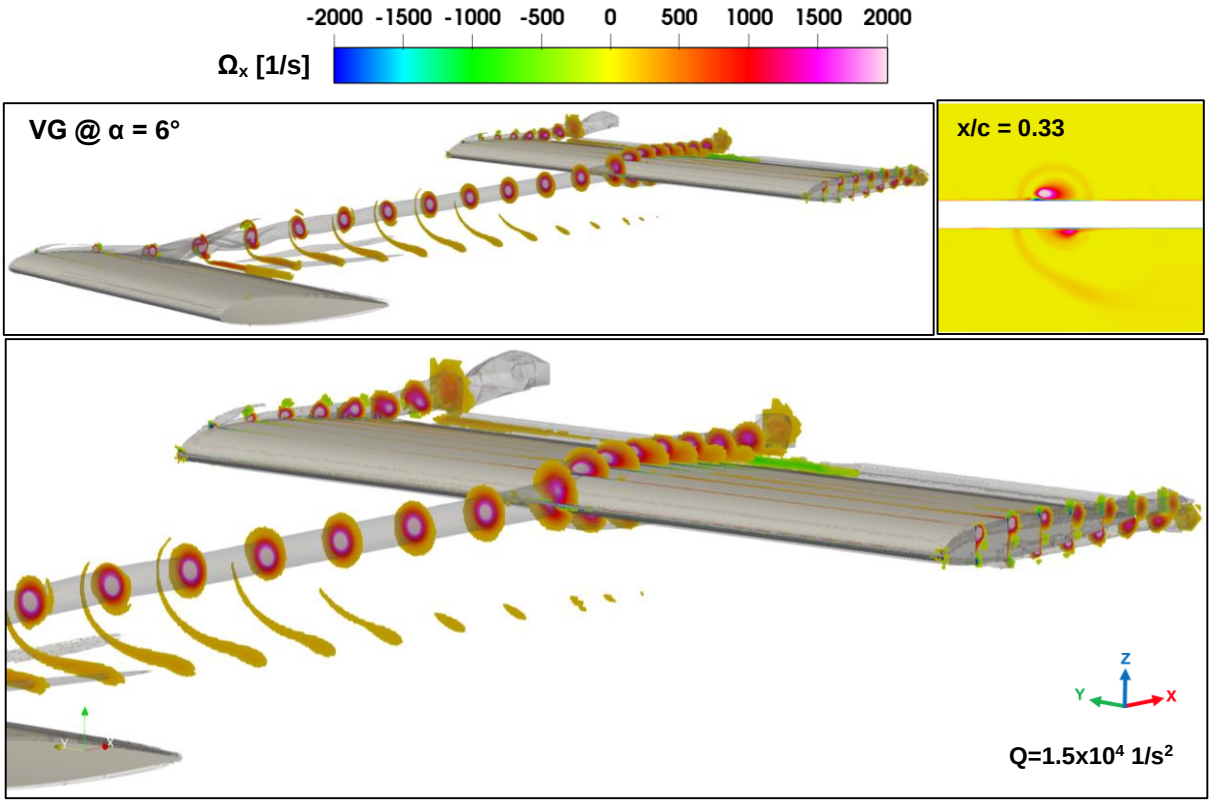

Figure 12: X-component of vorticity on y-z planes with VG at α = 6°

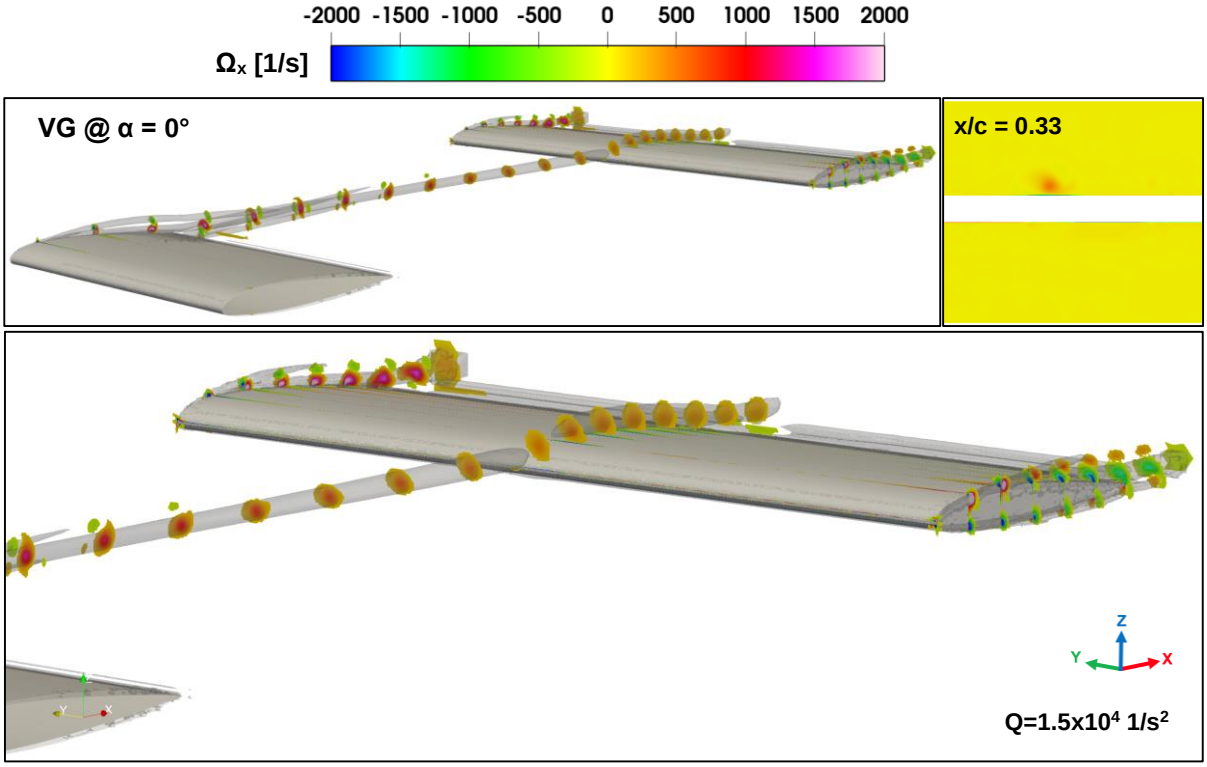

Figure 13: X-component of vorticity on y-z planes with VG at α = 0°

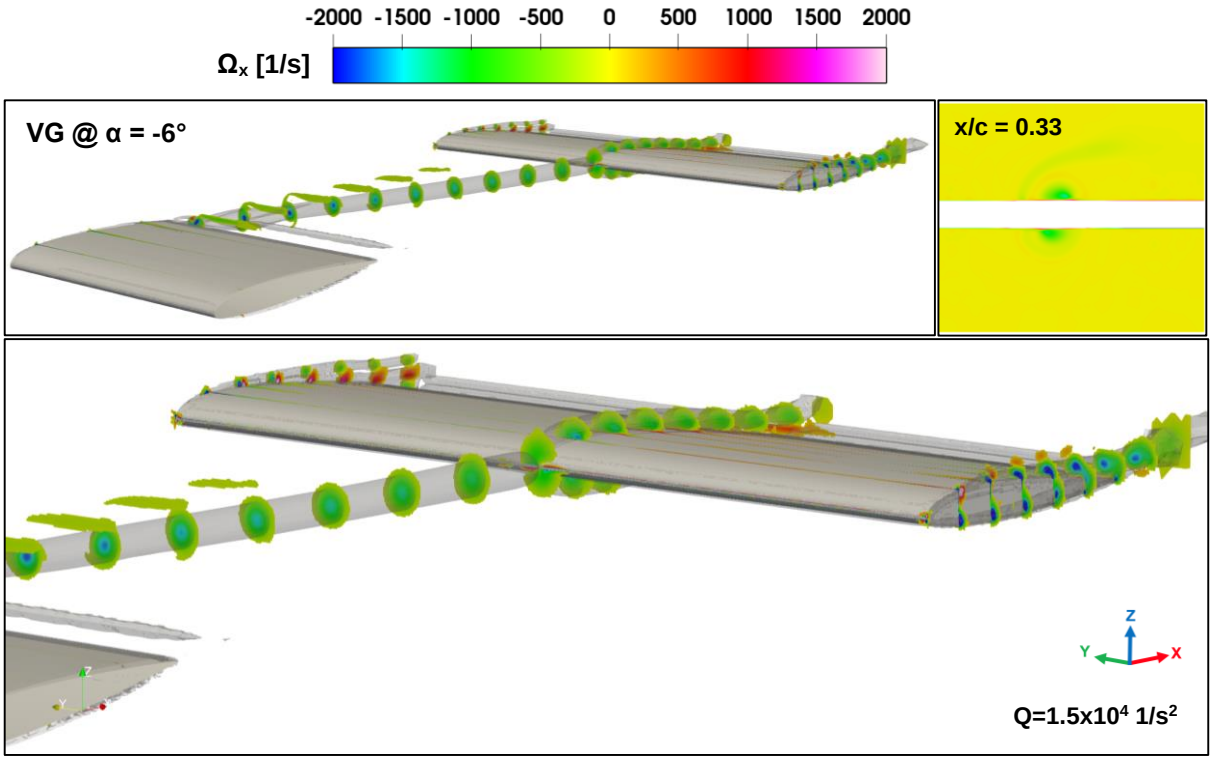

Figure 14: X-component of vorticity on y-z planes with VG at α = -6°

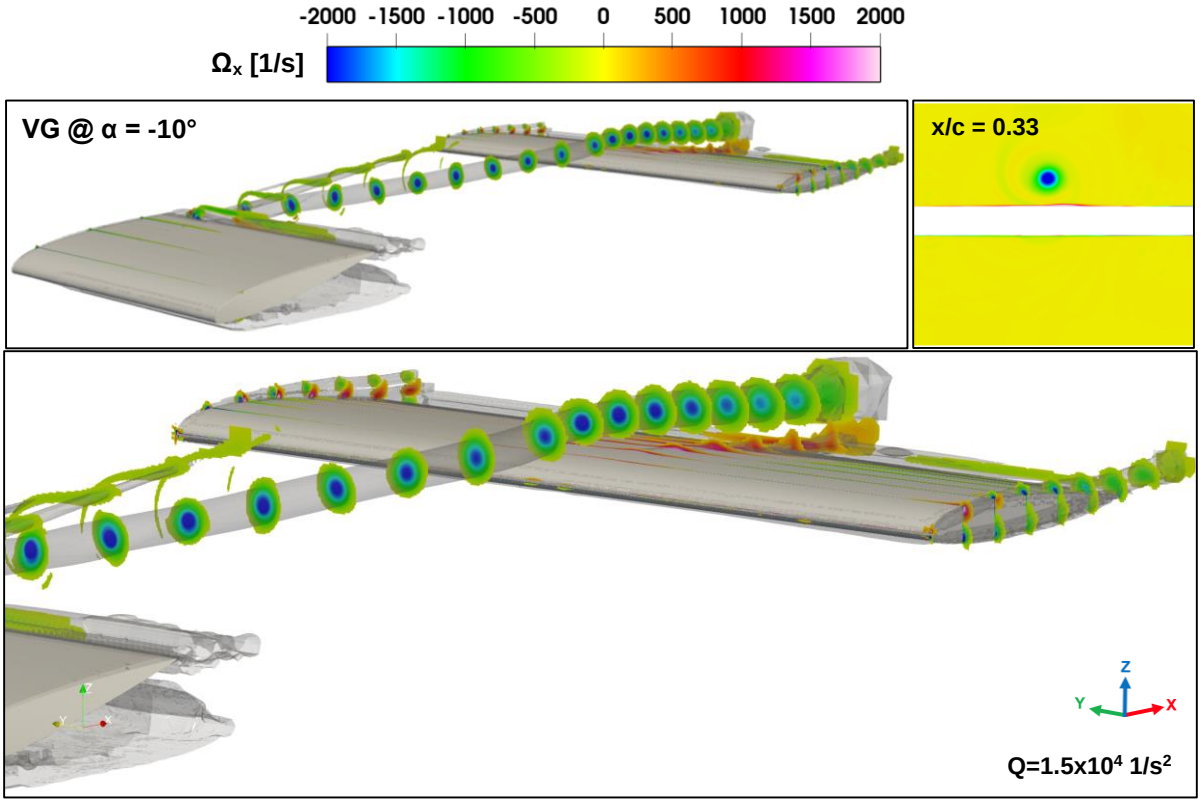

Figure 15: X-component of vorticity on y-z planes with VG at α = -10°

Among the positive angles of attack given in Figure 11 and Figure 12, Figure 11 demonstrates the strongest vortex core corresponding to the highest incidence of 10°. It is followed by the case shown in Figure 12 and the 0° case of Figure 13. A closer examination of the impinging

vortex reveals that, at higher angles of vortex generator, the majority of the induced flow impinges on the lower surface of the airfoil. This observation confirms that the upstream flow is redirected after passing the vortex generator, producing a pronounced downwash effect on the downstream. Such a mechanism is consistent with the findings of Droandi et al. [Droandi, Gibertini and Zanotti, 2016], who investigated light dynamic stall phenomenon in perpendicular blade–vortex interactions with an unsteady oscillatory airfoil. Their study also highlights the vortex trajectory generated by a vortex generator at 10° angle of attack. The similarity in vortex behavior underscores that the present simulations capture the essential dynamics of vortex formation, its propagation downstream and impingement on the surface, thereby demonstrating their reliability in reproducing the vortex–airfoil interaction mechanism.

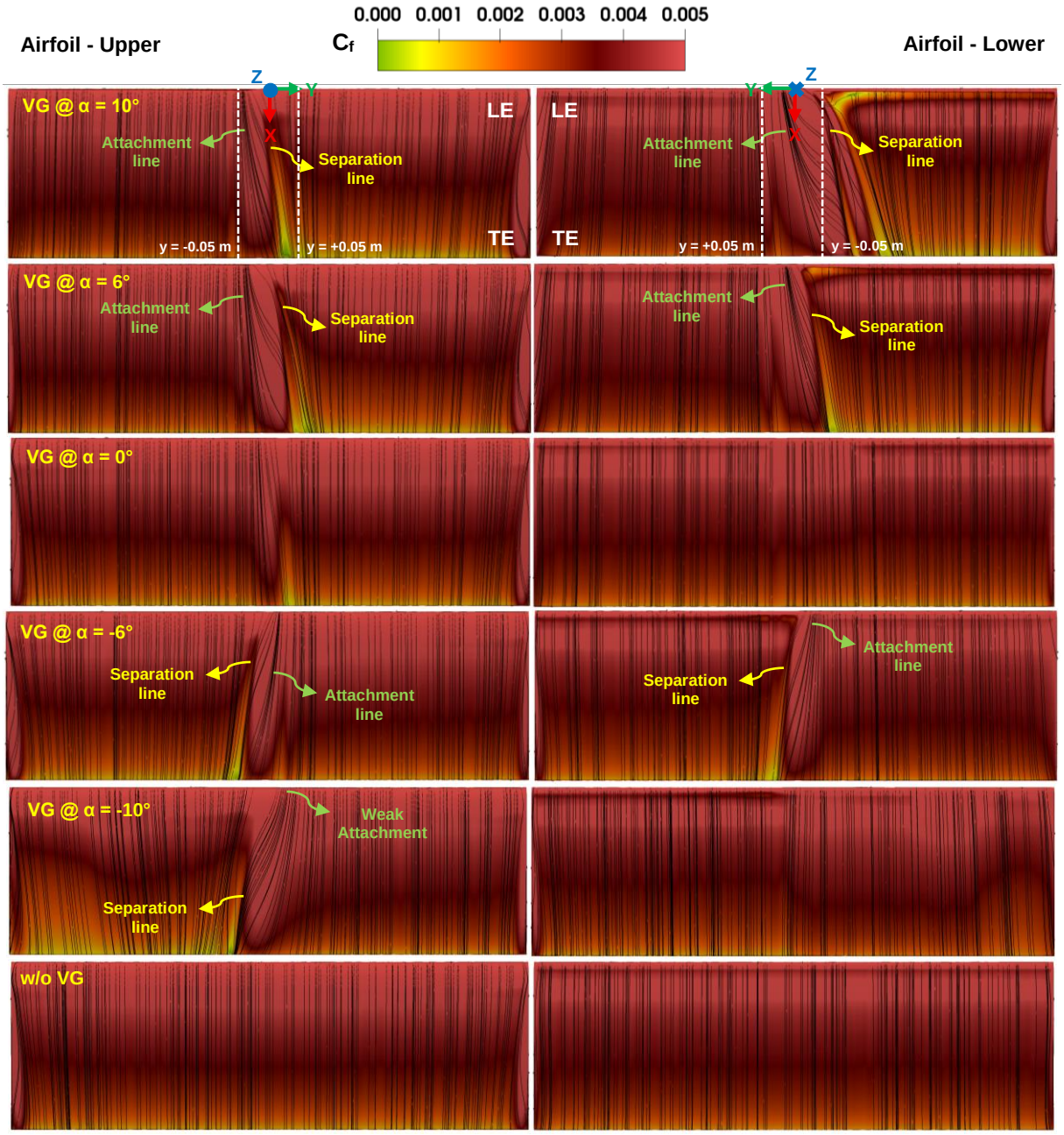

Figure 16: Skin friction coefficient distribution with streamlines on airfoil surfaces at different angles of attack

Figures 14 and 15 present the vorticity contours for the negative angle-of-attack cases, where the vortex flow is dominated by a clockwise (CW) rotation. Compared to the positive-angle cases, the vortex core exhibits reduced strength, and the flow trajectory at equal magnitudes of angle is not symmetric. This asymmetry arises from the cambered geometry of the NACA23012 profile used for the vortex generator, which alters the pressure distribution differently for positive and negative angles of attack. At α = –10°, the vortex core is observed to travel slightly away from the upper surface of the airfoil, reducing its direct influence on surface loading and weakening the overall impingement effects.

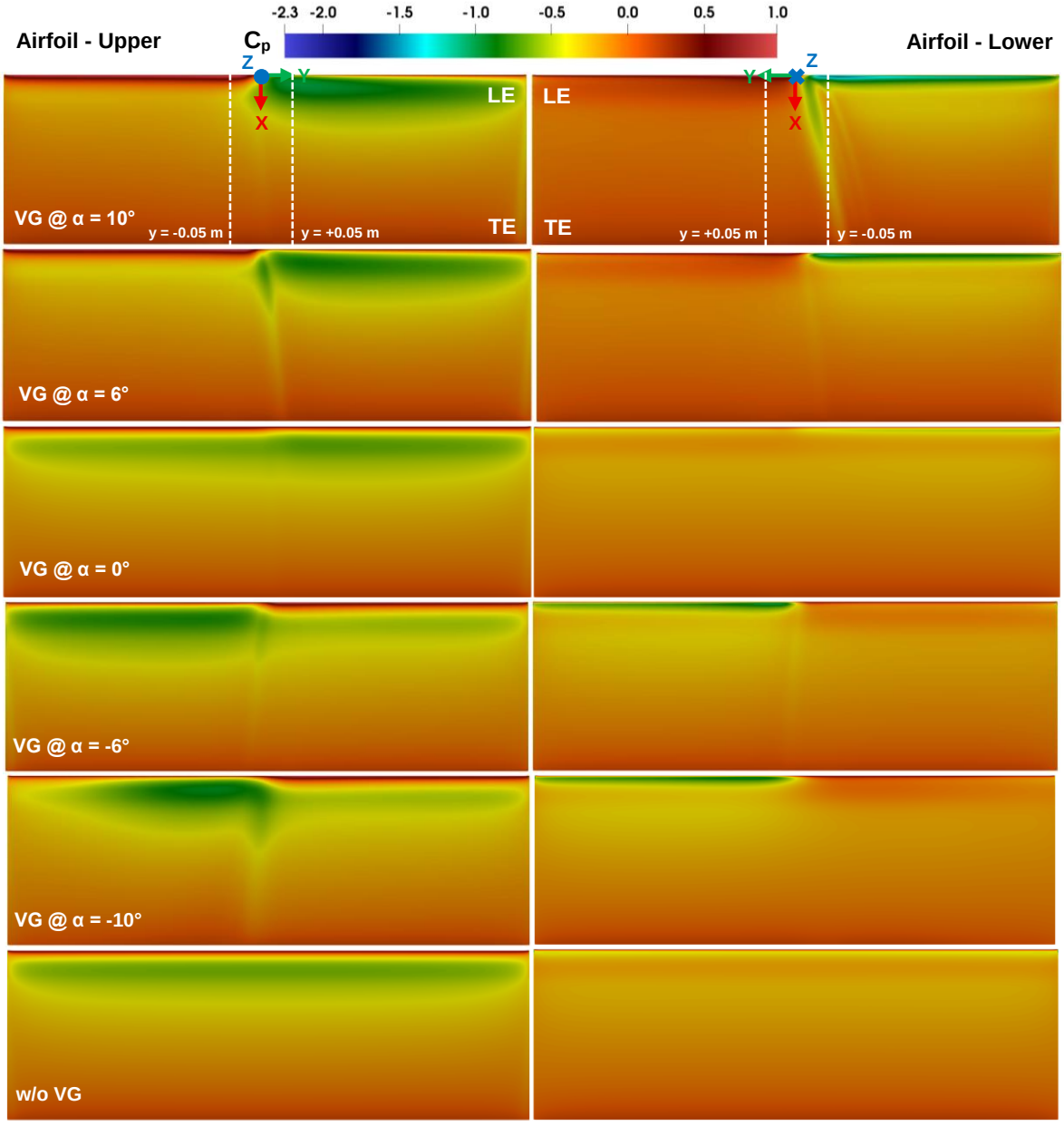

Figure 17: Pressure coefficient distribution on airfoil surfaces at different angles of attack

Figure 16 presents the skin friction coefficient contours on both the upper and lower surfaces of the airfoil, along with surface streamlines, with the free stream directed in the +x direction. The global coordinate system, the leading edge (LE) and trailing edge (TE) indicators are shown in the first contour and apply to all subsequent contours in the figure. Interpretation of streamlines and skin friction distributions under impinging vortex flow is inherently challenging; however, Seath and Wilson [Seath and Wilson, 1986] provide a useful framework through oil-

flow visualization in wind tunnel experiments. According to their observations, converging oil streaks indicate separation lines, while diverging streaks identify attachment lines. Since oil streaks represent surface streamlines, a similar approach is applied here. The streamlines on the airfoil are interpreted to locate the attachment and separation locations under the influence of vortex impingement. The skin friction coefficient contours in Figure 16 clearly reveal the footprints of the vortex on the airfoil surfaces. At the highest positive angle of attack of +10°, the vortex is deflected downward, producing strong impingement on the lower surface of the airfoil. In this region, distinct attachment and separation lines emerge which is showing the strong influence of the vortex. The skin friction coefficient is observed to be at its lowest value at the location corresponding to the separation line, as expected. On the upper surface, secondary footprints are also evident, indicating partial penetration of vortex effects. At moderate positive angle of attack ($\alpha = +6°$), these features weaken but remain present, with the vortex core shifting toward the upper surface as the downwash effect diminishes. Near zero angle, the vortex passes the airfoil with minimal surface interaction on the upper surface, and the skin-friction distribution remains nearly uniform on the lower surface. At the negative angle of attack of $\alpha = –6°$, the vortex is redirected upward, shifting the impingement footprints to the suction side of the airfoil and producing attachment and separation structures that are mirrored relative to its positive-angle counterpart. At $\alpha = –10°$, the effect of the vortex diminishes on the lower surface since the vortex core for this case was observed to be traveling slightly above the upper surface as shown in Figure 15, hence it has no interaction with the lower surface to cause an observable change in skin friction coefficient. Finally, the baseline flow without a vortex generator exhibits nearly uniform skin-friction and streamline patterns, confirming that the attachment and separation lines observed in other cases are solely induced by vortex impingement.

Figure 17 presents the pressure coefficient contours, which demonstrate that vortex impingement significantly alters the pressure distribution on both the upper and lower surfaces of the airfoil. Variations in the vortex trajectory at different vortex generator angles are directly responsible for the observed differences in surface loading. At the highest positive angle of attack ($\alpha = +10°$), the vortex produces strong impingement on the lower surface, creating a localized suction zone in the region subjected to flow separation under the influence of the swirling motion. Because the vortex rotates counterclockwise (CCW), suction is established on the right-hand side of the separation line on the lower surface, while the left-hand side of the attachment line experiences increased surface pressure, leading to a localized loading enhancement. A similar effect is also observed on the upper surface, though with reduced magnitude. As the angle of attack decreases, the same mechanisms remain active, but their influence weakens. At $\alpha = 0°$, the vortex passes the airfoil with minimal interaction, resulting in less gradients on the upper surface and an almost uniform pressure coefficient distribution on the lower surface. In fact, the effect of angle of $\alpha = 0°$ is very similar to the case without the vortex generator. For the negative angles of attack ($\alpha = –6°$ and $–10°$), the vortex rotates clockwise (CW), reversing the behavior: a suction zone forms on the left side of the separation line on the lower surface, while the right side of the attachment line here is subjected to higher pressure, producing a mirrored loading pattern relative to the positive-angle cases.

The skin friction and pressure coefficient distributions are further examined in x–z planes selected at $y = +0.05$ m and $y = –0.05$ m that are chosen to capture the region where the vortex trajectory passes through. According to Figure 18, the distributions of the skin friction coefficient on these planes (top row) represent the locations of separation and attachment zones. In Figure 16, it was observed that the value of this coefficient was decreasing at the locations corresponding to where flow separation occurs. Hence, the chordwise variations shown here reflect this. Since the most significant gradients at these particular two locations are observed to occur at $\alpha = +10°$, the skin friction coefficient shows more observable variations in these two graphs for this case compared to the baseline which has no vortex generator. Especially at $y = –0.05$ m, a distinct increase in skin friction coefficient is observable along the chord beyond $x/c = 0.3$, which is the result of the separation line formed by the impingement of the vortex.

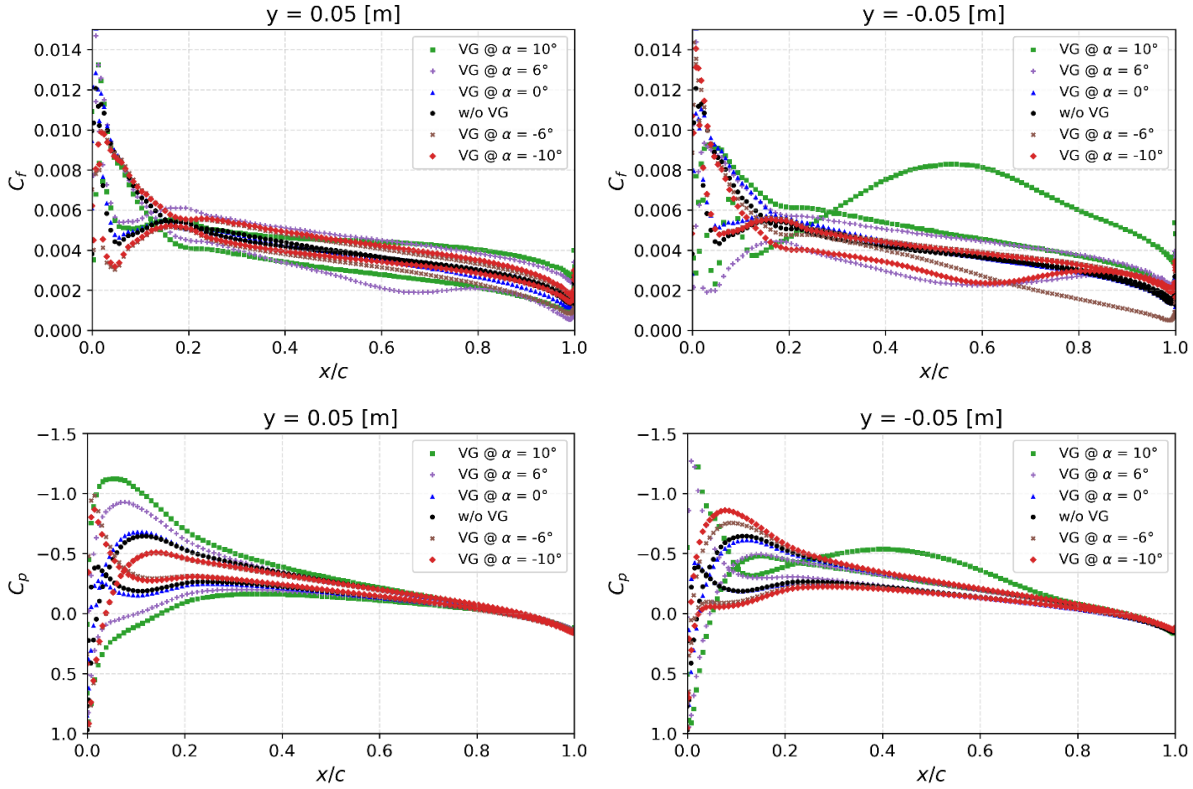

Figure 18: Comparisons along the chord of the airfoil at y = ±0.05 m, top row: skin friction coefficient, bottom row: pressure coefficient

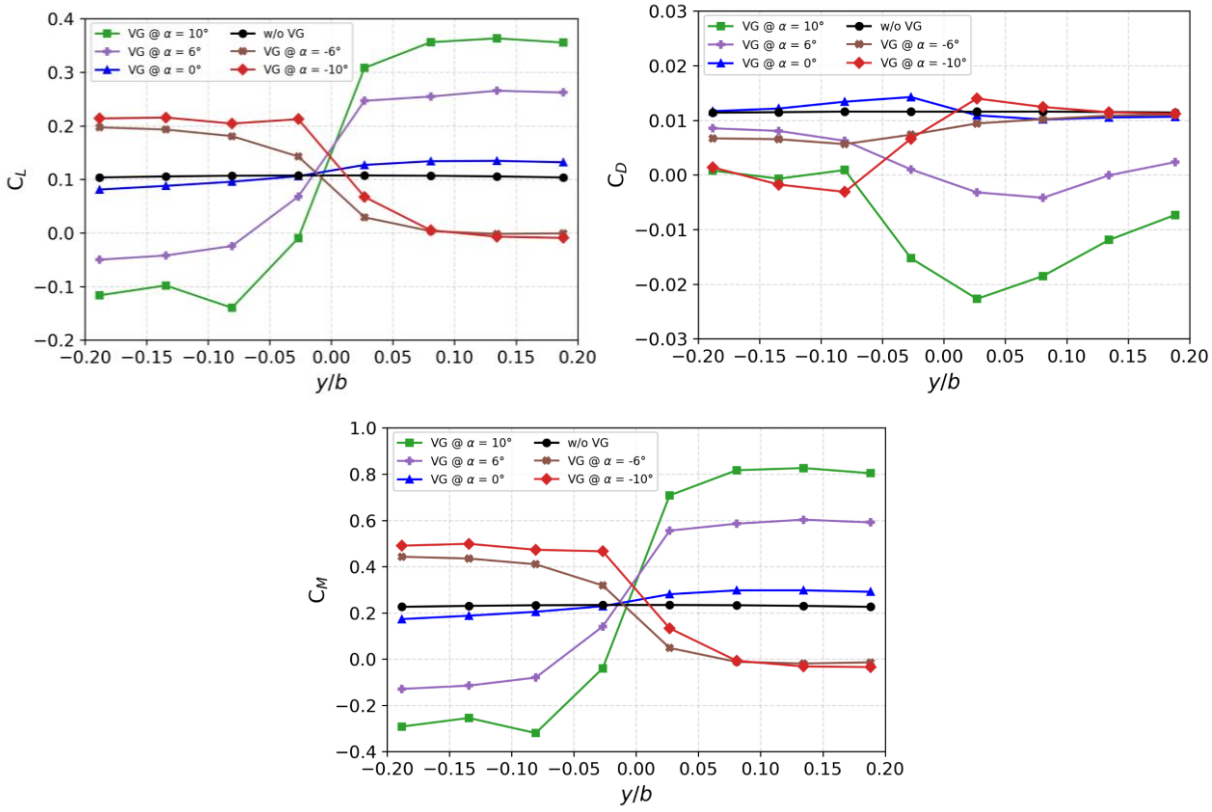

Figure 19: Distribution of aerodynamic coefficients along the airfoil span at different angles of attack

The pressure coefficient distributions in Figure 18 (bottom row) further illustrate the influence of the vortex impingement on the airfoil. At α = +10°, the vortex interaction enhances the pressure difference between the upper and lower surfaces at y = +0.05 m, thereby supporting an increase in lifting force. At y = –0.05 m, however, the upper surface of the airfoil experiences localized loading from the impinging vortex around x/c = 0.13, while the lower surface is subjected to suction. This combination reduces the pressure differential across the section and leads to a local decrease in lift. For the negative angle of attack of α = –10°, the described effects are more or less reversed, but with a lessened magnitude due to both the reduced vortex strength and the influence of the cambered airfoil geometry. At α = 0°, the vortex passes the airfoil with minimal interaction, resulting in an almost the same pressure distribution with the airfoil in the absence of the vortex generator.

Finally, Figure 19 illustrates the aerodynamic performance of the airfoil under the studied flow conditions. The aerodynamic forces acting on an airfoil's surface are a result of the pressure and shear stress distributions on that surface, which were demonstrated so far in terms of coefficients of pressure and skin friction. The coefficients of lift, C_L, drag, C_D, and moment, C_M, are evaluated for a spanwise section between y/b = 0.2 and y/b = -0.2, where b is the span of the airfoil. This region is of particular interest as it includes the interval where the vortex is observed. C_M is the moment about the quarter chord, which is the aerodynamic center of this cambered airfoil. It is observed that the trends of C_L and C_M are closely related, as the strong vortex–airfoil interactions primarily influence the region between the leading edge and the aerodynamic center. In contrast, C_D exhibits different trends for the cases considered, reflecting the localized attachments and separations induced by the impinging vortex.

CONCLUSION

In this study, a perpendicular BVI case is examined by simulating a vortex generator and an airfoil positioned downstream of the generator, and the results from steady-state CFD analyses are presented. In order to capture the intricate flow features of the vortex interaction with the aerodynamic surface, a highly refined grid is used. To reduce spatial discretization error of the simulation, a grid sensitivity study is employed. The analyses show that the grid resolution that was selected for the particular boundary conditions under investigation is sufficient to capture the essential vortex–airfoil interaction physics. A detailed investigation of this interaction is performed through a series of simulations with varying the angle of attack of the vortex generator incrementally between +10° and -10°. The simulations are analyzed thoroughly to demonstrate the effects of the interaction phenomenon on and around the downstream airfoil geometry in terms of static pressure, skin friction, and the vortex field.

Results demonstrate that the angle of attack of the vortex generator strongly governs the vortex strength, trajectory, and rotational direction, which in turn determine the location and intensity of vortex impingement on the airfoil surfaces. Positive angles are observed to be deflecting the vortex downward, enhancing loading on the lower surface, while negative angles shift the impingement to the upper surface with weakened effects. The distributions of surface pressure and skin friction coefficients confirm the presence of distinct attachment and separation lines induced solely by vortex impingement. Consequently, these effects are also observed in the trends of the calculated aerodynamic coefficients.

References

ANSYS, Inc., (2024) ANSYS Fluent Theory Guide, Release 2024 R2, Canonsburg, PA, USA.

Chen, J. M., and Chiou, C. C. (1998) Experimental Investigation of a Parallel Vortex–Plate Interaction, Journal of Fluids and Structures, Vol.12, p: 295-314, 1998.

Celik, I. B., Ghia, U., Roache, P. J., Freitas, C. J., Coleman, H., and Raad, P. E. (2008) Procedure for Estimation and Reporting of Uncertainty due to Discretization in CFD Applications, ASME Journal of Fluids Engineering, Vol.130, No. 7, 2008.

Colli, A., Abbà, A., and Gibertini, G. (2022) Experimental and Numerical Study of Parallel Blade–Vortex Interaction, 48th European Rotorcraft Forum, 2022-0096, 2022.

DeSpirito, J. (2016) CFD Validation of Interaction of Fin Trailing Vortex with Downstream Control Surface in High Subsonic Flow, AIAA SciTech Forum, 2016-1546, 2016.

Droandi, G., Gibertini, G., and Zanotti, A. (2016) Perpendicular Blade-Vortex-Interaction over an Oscillating Airfoil in Light Dynamic Stall, Journal of Fluids and Structures, Vol. 65, p: 472-494, 2016.

Garmann, D.J., and Visbal, M.R. (2015) Interactions of a Streamwise-Oriented Vortex with a Finite Wing, Journal of Fluid Mechanics, Vol. 767, p: 782–810, 2015.

Luckring, J. M., and Rizzi, A. (2024) Prediction of Concentrated Vortex Aerodynamics: Current CFD Capability Survey, Progress in Aerospace Sciences, Vol. 147, 2024.

Omar, A.A., Chongam, K., and Oh-Hyun, R. (2002) Numerical Simulation of the Vortex-Fin Interaction over a Tangent-Ogive Cylinder, The Aeronautical Journal, p: 175–180, 2002.

Seath, D. D., and Wilson, D. R. (1986). *Vortex-Airfoil Interaction Tests*, AIAA 24th Aerospace Sciences Meeting, 1986-0354, 1986.

Spalart, P. R., and Allmaras, S. R. (1994) A One-Equation Turbulence Model for Aerodynamic Flows, La Recherche Aérospatiale, No. 1, p: 5–21, 1994.

Spalart, P. R. and Shur, M. L. (1997) On the Sensitization of Turbulence Models to Rotation and Curvature, Aerospace Sci. Tech., Vol. 1, No. 5, p: 297–302, 1997.

Shur, M. L., Strelets, M. K., Travin, A. K., and Spalart, P. R. (2000) Turbulence Modeling in Rotating and Curved Channels: Assessing the Spalart-Shur Correction, AIAA Journal, Vol. 38, No. 5, 2000.

Sun, Z., Gu, Y., and Zhao, H. (2019) Experimental Investigation on the Streamwise Vortex–Surface Interaction, Journal of Visualization, Vol. 22, p: 477–488, 2019.

Werner, M., Rein, M., Richter, K., and Weiss, S. (2023) Experimental and Numerical Analysis of the Aerodynamics and Vortex Interactions on Multi-Swept Delta Wings, CEAS Aeronautical Journal, Vol: 14, p: 927–938, 2023.

Wittmer, K.S., Devenport, W.J., Rife, M.C., and Glegg, S.A.L. (1995) Perpendicular Blade Vortex Interaction, AIAA Journal, Vol. 33, No. 9,1995.